Dalton Transactions

Accepted Manuscript

ROYAL SOCIETY OF CHEMISTRY

www.rsc.org/dalton

Two in one: Switchable ion conductivity and white light emission integrated in an iodoplumbate-based twin chain hybrid crystal

Hai-Bao Duan,[a,b] Shan-Shan Yu,[a] Yuan-Bo Tong,[b] Hong Zhou[a] and Xiao-Ming Ren*[b,c,d]

[a] School of Environmental Science, Nanjing Xiaozhuang University, Nanjing 211171, P. R. China

[b] State Key Laboratory of Materials-Oriented Chemical Engineering and College of Science, Nanjing Tech University, Nanjing 210009, P. R. China

[c] College of Materials Science and Engineering, Nanjing Tech University, Nanjing 210009, P. R. China

[d] State Key Laboratory & Coordination Chemistry Institute, Nanjing University, Nanjing 210093, P. R. China

Tel.: +86 25 58139476

Fax: +86 25 58139481

E-mail: xmren@njtech.edu.cn

Abstract

An iodoplumbate-based hybrid, $[C_7\text{-Apy}][PbI_3]$ (**1**), where $C_7\text{-Apy}^+$ = 1-heptyl-4-aminopyridinium, was prepared using a simple solution process. Three sequential phase transitions undergo in 402-443 K. In both the lowest and highest temperature phases, hybrid crystal **1** is comprised of discrete $[Pb_2I_6]_\infty$ twin chains, which are surrounded by $C_7\text{-Apy}^+$ cations. The connectivity between PbI_6 octahedra within a $[Pb_2I_6]_\infty$ twin chain and the arrangement of cations are quite difference between lowest- and highest-temperature phases. Hybrid **1** shows switchable ion conductivity due to the structural phase transition and white light emission attributed to the broadband semiconductor emission of twin chain. The former functionality has potential application in ion conductor device; the single-phase white light emitter is useful material in the low-cost and easily fabricating high-efficiency white lighting-emitting diodes.

Keywords: Iodoplumbate-based hybrid; Ion conductor; White-light-emission; Switchable conductivity

Introduction

Interest is growing in the research area of haloplumbate-based hybrids, this is due to their tunable structures from the discrete mononuclear or polynuclear species (zero-dimensional; abbr. 0-D) to infinite variety with higher dimensionality[1-8] (one-dimensional,[1,3-6] two-dimensional[7,8] or three-dimensional[2]; hereafter abbr. as 1-D, 2-D and 3-D, respectively) and a wide range of novel physical properties from optics[9-13] to electronics.[14-16]

In haloplumbate-based hybrid context, the perovskite-type ones have being attracted tremendous research interesting. The 3-Dhaloplumbate-based perovskites, $CH_3NH_3PbI_{3-x}Cl_x$, with much lower exciton binding energies and intense light absorption over the whole visible light region, have been employed as absorbers in solar cells. It is remarkable that the records of certified power conversion efficiencies have being constantly refurbished and it is over a time of merely a few years that the power conversion efficiency was enhanced up to 20%.[14] Most recently, the $CH_3NH_3PbI_{3-x}Cl_x$perovskites have being discovered to show amazing bipolar and bistable resistive switching behavior with small on-off voltage of <1.0 V in a simple metal-dielectric-metal capacitor configuration device of $Au/CH_3NH_3PbI_{3-x}Cl_x$/fluorine-doped tin oxide substrate, revealing their additional promising application in the nonvolatile memory device field.[17] The 2-D haloplumbate-based hybrid, (N-MEDA)$[PbBr_{4-x}Cl_x]$ (N-MEDA = N1-methylethane-1,2-diammonium, x = 0-1.2), are single-phase white-light emitters, and their broadband emission across the entire visible spectrum arises from corrugated lead halide sheets. Interestingly, the emission is tunable through halide substitution to afford both “warm” and “cold’ white light in such haloplumbate-based wide-band gap semiconductors.[9] The 1-D iodoplumbate-based hybrids were reported to display ferroelectricity, where the polarization is switchable under an alternating current electrical field.[18]

In addition, a 3-D open-framework hybrid, $(EDAMP)_{2n}(Pb_7I_{18})_n \cdot 4nH_2O$ ($EDAMP^{2+}$ = $Et_2NHC_6H_4$-$CH_2C_6H_4NHEt_2$), which inorganic framework is built from

purely octahedral PbI_6units and behaves as a quantum-wire array, shows fascinating wavelength-dependent photochromic behavior.[19] Its color changes from yellow to olive green under illumination with λ = 500 nm light and further to dark green with light of λ<500 nm. Most interestingly, the reversion of the color for the hybrid can be accomplished by heating, indicating that this hybrid possesses switchable photochromic nature. It is well known that a material, with switchable functionality through the external stimuli, such as thermally triggered, irradiation inducing and applied pressure, is very useful for the application in the fields of sensor, memory and data storage.[20-23]

In this paper, we report on an iodoplumbate-based hybrid, $[C_7\text{-Apy}][PbI_3]$ (**1**) where $C_7\text{-Apy}^+$= 1-heptyl-4-aminopyridinium, which shows fascinatingly switchable ion conductivity and white light emission.

Results

The yellowish needle-shaped crystals of **1** were achieved by slowly evaporating a DMF solution containing PbI_2, KI and $[C_7\text{-Apy}]Br$. The hybrid crystals were insoluble in common organic solvents, besides DMF and DMSO, as well as water. The purity was examined for **1**using elemental analyses for C, H and N and powder X-ray diffraction technique (Figure S1). This hybrid is thermally stable up to ca. 300 °C (ref. Figure S2).

Ionic conductivity. The ion conductivity of **1** was measured by AC impedance spectroscopy under dry N_2. The AC frequencies span from 1 to 10^7 Hz. The corresponding Nyquist plots between 333 and 415 K are displayed in Figure 1a and Figure S3. Below 373 K, the -Z'' vs. Z' plot shows a pitch arc, indicating the existence of high resistance owing to the ions are immovable in crystal lattice; and above 373 K, each Nyquist plot at selected temperature shows a semicircle and the semicircle diameter becomes smaller with increasing temperature. At higher temperatures (above 373K), two semicircles appear in the complex impedance plots in the high frequency region, although these plots look to give single semicircle if have a glance at them (ref. Figure S3b). Two semicircles in the complex impedance plots correspond to the bulk

and grain boundary resistances of the powdered crystals.[24,25] The complex impedance data at selected temperatures were fitted using an equivalent circuit (EC) consisting of two series of parallel RC (Resistance and Capacitance) circuits.[26-28] The best fits gave, for instance, $\sigma = 7.93\times10^{-9}$ S·cm^{-1} at 393 K and 8.55×10^{-7} S·cm^{-1} at 403 K. The temperature dependent conductivities (σ) are plotted in the form of logσ vs. 1000/T, showing linear relationship in the temperature range of 333-393 K and 403-413 K (ref. Figure1b), respectively; the activation energy was estimated to be 1.348 eV. Surprisingly, as the temperature increased, the electrical conductivity sharply increases about two orders of magnitude and reaches to 8.55×10^{-7} S·cm^{-1} at 403 K, and the conductivity continuously increase in the temperature ranges of 403-413 K with rising temperature and the corresponding activation energy was estimated to be 1.078 eV, being slight less than that in LT phase.

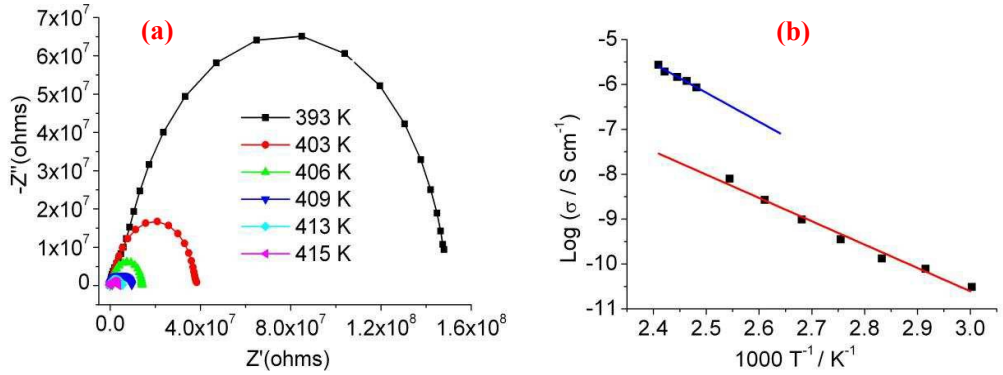

Figure 1 (a) Complex impedance between 393 and 415 K (b) Arrhenius plots between 333 and 413 K for **1**.

Dielectric behavior. In the ion-type hybrid crystal **1**, the applied electrical field probably induces the dipole motions, which include intrinsic dipole orientated motions and ion relatively displacing motions. Besides the electron transport, the conduction of **1** is also contributed from the dipole motions in the AC impedance measurement. In order to investigate the dipole motion in **1**, its dielectric behavior was further analyzed.

The dielectric permittivity (ε′) and loss (tan(δ))as a function of frequency is displayed in Figure 2 as well as the ε′ and tan(δ) as a function of temperature is shown

in Figure S4for **1** at selected temperatures. The ε′ value is less than 9.0 at low frequency (f = 1 Hz) and is almost constant (ε′ ≈ 7.3) in the high frequency region (f > 10^3 Hz) when the temperature is below 323 K. At high temperatures, the dielectric permittivity drops rapidly with increasing frequency to 10^3 Hz (when the temperature is below 383 K) or 10^5 Hz (when the temperature is above 393 K; ref. Figure 2a) in the plot of ε′ vs. frequency. These results indicate that the dynamic dipole motion cannot follow the quick switching of the applied electrical field at higher frequencies. Meanwhile, as shown in Figure 2b, a dielectric loss peak becomes visible at the temperature above 343 K. The maximum of the dielectric loss peak in the plot of tan(δ) vs. frequency shifts toward higher frequencies with increasing temperature, demonstrating the existence of thermally active dielectric relaxation. Dielectric relaxation originating from electronic transitions or molecular vibrations has a frequency above 10^{12} Hz, while slow dielectric relaxations originating from dipole orientation motion or ionic displace polarization occur in the range of 10^2–10^{10} Hz. The frequency of dielectric relaxation in **1** falls within the regime of the dipole orientation or ionic displace polarization relaxation mechanism, revealing that the thermally active dielectric relaxation in **1** is related to the dynamic dipole orientation and ionic displace polarization motion that gives rise to ion conductance.

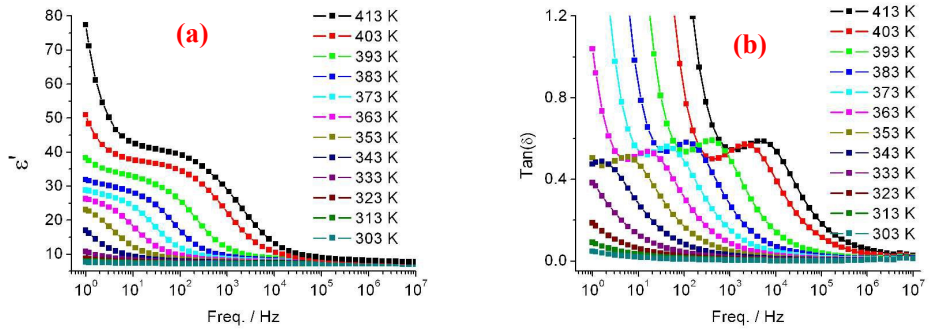

Figure 2 Frequency dependent dielectric permittivity (a) real and (b) imaginary parts at selected temperatures for **1**.

DSC analysis. To reveal the novel switchable ion conductivity of **1**, we performed the DSC measurement in the temperature ranges of 193-483 K, and observed three thermal anomaly events in the heating run (Figure 3), indicating the existence of three

sequential phase transition. Three thermal anomalies are close to each other, the onset temperature occurs at ca. 402 K for the thermal event in the low-temperature side. Interestingly, only one exothermic peak (T_{peak} = 359 K) appears in DSC plot in the cooling run, and such a phenomenon is analogous to the frequent observations in ion-liquid crystals,[29] which is related to that the thermal motion of the alkyl chains cannot follow the temperature change during the heating-cooling cycle.

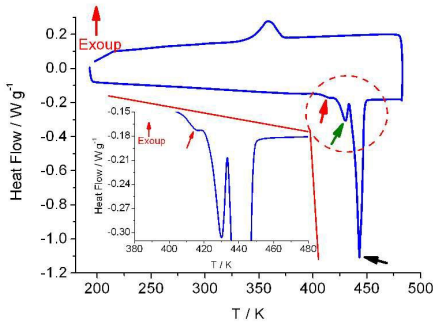

Figure 3 DSC plot of **1** showing three anomalies upon heating and one exothermal event upon cooling.

Crystal structures. In line with the DSC analysis, we collected the X-ray single crystal diffraction data at 296, 393 K in the lowest temperature (LT) phase and at 421 K in highest temperature (HT) phase to determine the crystal structures. Hybrid **1** crystallizes in orthorhombic space group *Pbcn* in LT phase; an asymmetric unit is comprised of two distinct Pb^{2+} ions and six different I^- ions together with two inequivalent C_7-Apy^+ cations (Figure 4a and 4b); all atoms occupy general positions. Pb(1) and Pb(2) form the distorted PbI_6 coordination octahedra, respectively, where four I^- ions lying on the equatorial plane and one I^- ion locating at the axial site are shared out and referred to as bridging iodides; one I^- ion in the axial position of octahedra undergo no sharing and is called the terminal iodide (I(2) in Pb(1) coordination octahedron and I(5) in Pb(2) coordination octahedron are called terminal iodides). In the $Pb(1)I_6$ coordination octahedron, I(1) occupies two equatorial positions and I(3) and I(4) the other two equatorial positions, I(2) and I(6) occupy two axial position. In the $Pb(2)I_6$ coordination octahedron, I(6) occupies two equatorial

positions and I(3) and I(4) the other two equatorial positions, I(1) and I(5) occupy two axial position. At 296 K, the coordination geometry of Pb^{2+} ion shows the equatorial Pb-I bond distances to be similar in the ranges of 3.1380(9)-3.2691(8)Å within the $Pb(1)I_6$ coordination octahedron and of 3.0950(9)-3.3097(8) Å within the $Pb(2)I_6$ one, whereas two axial Pb-I bond distances are the longest ($d_{Pb(1)-I(6)\#1}$ = 3.5016(8) and $d_{Pb(2)-I(1)\#2}$ = 3.5446(9) Å; symmetric codes: #1 = x, -1+y, z; #2 = x, 1+y, z) and shortest ($d_{Pb(1)-I(2)}$ = 3.0477(8) and $d_{Pb(2)-I(5)}$ = 3.0416(8) Å), respectively. The $Pb(1)I_6$ and $Pb(2)I_6$ octahedra share one base-to-apex edge, made up of I(1) and I(6), to form a $Pb_2I_6^{2-}$ subunit; the neighboring subunits are connected into a twin chain of $\{Pb_2I_6\}_\infty$ along b-axis via sharing corner (μ_2-I(4)) and triangular face (I(1)-I(3)-I(6)); the relative rotation occurs between the equatorial planes of the neighboring $Pb_2I_6^{2-}$ subunits (for instance, the dihedral angle is 52.4° between two I(1)-I(1)-I(4)-I(3) planes versus 50.7° between two I(6)-I(6)-I(3)-I(4) planes). Such an anionic twin chains are rarely seen in the lead iodide hybrids.[30]

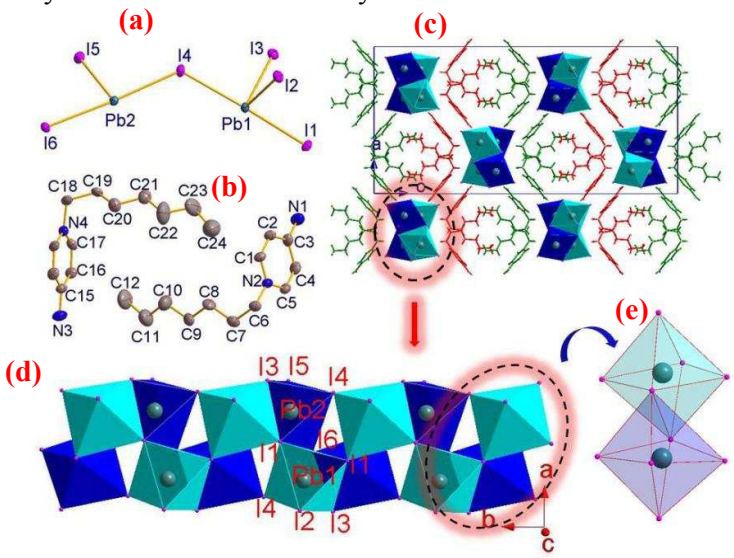

Figure 4 (a, b) An asymmetric unit with non-H atomic labeling (where H atoms are omitted for clarity) (c) packing diagram viewed along the b-axis (d) an anionic twin chain where Pb_2I_6 subunit is labeled for **1** in LT phase (at 296 K).

Two inequivalent cations adopt the bent conformation, alkyl chain slightly disrupted close to the pyridyl ring with an almost completely trans-planar conformation. At 296 K, the charge-assisted H-bonding interactions appear between

the NH_2 groups and the I^- ions with the parameters $d_{H(1B)\ldots I(2)\#3}$ = 3.024, $d_{H(3A)\ldots I(5)\#4}$ = 3.025 and $d_{H(3B)\ldots I(4)}$ = 2.892 Å (ref. Figure S5 and symmetric codes: #3 = 1.5-x, 0.5+y, z and#4 = x, 2+y, z). The π…π stack occurs between two adjacent pyridyl rings containing N(3) atom, with a dihedral angle of 10.4° and the shorter interatomic distances $d_{C(15)\ldots C(17)\#6}$ = 3.396, $d_{C(16)\ldots C(16)\#6}$ = 3.200 Å (ref. Figure S6 and symmetric code: #6 = 1-x, y, 1.5-z). The packing diagram of **1** viewed along b-axis is shown in Figure 4c.

The crystal structure of **1** at 393 K (in LT phase) is quite analogous to that at 296 K. From 296 to 393 K, the a- and b-axes expand respectively by 1.46% and 1.18%, and the cell volume increases by 1.61%, while the c-axis shrinks by 1.03%. The typical bond parameters in the crystal structures at 393 K, shown in Table S2 and S3, are in good agreement with those at 296 K, whereas the displacement parameters are obviously larger than those at 296 K.

Upon heating from 393 K to 421 K, the structural phase transition underwent in the hybrid crystal of **1**. It is notable that with respect to 296 K, the reduced cell volume increases by ca. 1.6% from 296 to 393 K (with the temperature interval ΔT = 98 K) in LT phase while by ca. 3.0% from 393 to 421 K (with the temperature interval ΔT = 28 K) across the structural phase transition. Besides this, the space group switches from *Pbcn* in LT phase to P-1 in HT phase (ref. Table S1). This is an extraordinary situation that the structural phase transition leads to the lattice possessing higher symmetry in LT phase.

In HT phase, the asymmetric unit is still comprised of two distinct Pb^{2+} ions and six different I^- ions with two C_7-Apy^+ cations (Figure 5a and 5b). Two distinct Pb^{2+} ions also are all situated in a distorted octahedral coordination environment. At 421 K, the Pb-I distances fall in the ranges of 3.0241(18)-3.4156(15) Å in Pb(1) coordination octahedron versus 3.0106(18)-3.6093(16) Å in Pb(2) coordination octahedron. With respect to the crystal structure in HT phase, the Pb(1) and Pb(2) coordination octahedra show much heavily distorted in LT phase.

Between LT and HT phases, the noteworthy changes of crystal structures of **1** concern the aspects (1) as shown in Figure 4b, 5b and Table S3, the equivalent and

anisotropic displacement factors in the inorganic units $[Pb_2I_6]^{2-}$ and the 4-NH_2Py moieties at 421 K in HT phase are comparable to those at 393 K in LT phase, whereas the alkyl chains exhibit heavily disordered in HT phase. (2) The relative orientation between neighboring cations is significant distinction (Figure 4c and 5c-5e). The neighboring cations show staggered arrangement (ref. Figure 4c, where the cations are in red color or olive color) in LT phase while head-to-tail alignment (ref. Figure 4c, where the cations are in red color or olive color) in HT phase when viewed along the inorganic chain direction. (3) For the inorganic $\{Pb_2I_6\}_\infty$ twin chain, the connectivity of $Pb(1)I_6$ coordination octahedra is difference. As shown in Figure 5f, each Pb(1)/Pb(2) coordination octahedron, in LT phase, is connected to two equivalent Pb(1)/Pb(2) coordination octahedra via sharing an apex, and three equivalent Pb(2)/Pb(1) coordination octahedra via sharing an apex, an edge and a triangle face, respectively. Whereas each Pb(1)/Pb(2) coordination octahedron, in HT phase, is connected to one Pb(1)/Pb(2) coordination octahedron and four Pb(2)/Pb(1) coordination octahedra, amongst them, each Pb(1)/Pb(2) coordination octahedron are linked to one Pb(1)/Pb(2) coordination octahedron and three Pb(2)/Pb(1) coordination octahedra via sharing one edge, one Pb(2)/Pb(1) coordination octahedron via sharing an apex, which is displayed in Figure 5g.

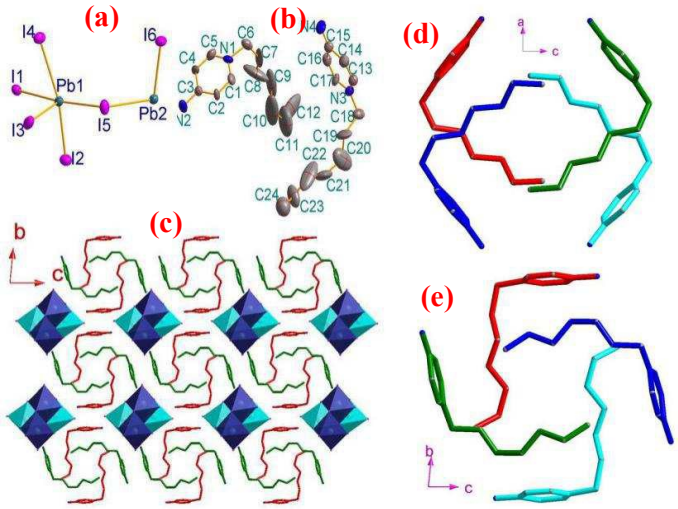

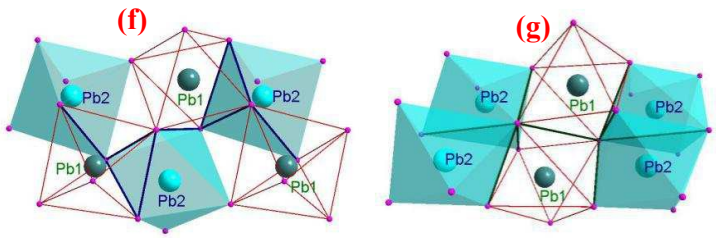

Figure 5 (a, b) Asymmetric unit with non-H atom labeling of **1**, the anomaly ellipsoids of C atoms in alkyl chain is due to structurally disordered where H atoms omitted for clarity (c) packing structure viewed along a-axis in HT phase (d, e) cation arrangements in LT and HT phases viewed along the inorganic chain direction. And coordination polyhedral connectivity in (f) LT and (g) HT phases, where the shared edges are marked by navy thick bonds.

Absorption and Photoluminescence spectra. Figure 6 shows the solid state optical absorption spectrum of **1** at room temperature. Two intense absorption bands centered at 226 and 302 nm appear in the spectrum of **1** together with a shoulder around 285 nm and a broad band around 406 nm. The absorption bands with λ_{max}< 400 nm show the narrow half-peak and more intense with respect to the band around 406 nm, and these bands are assigned to the π*←π transition within the pyridyl ring of cation; the broad band around 406 nm arises from the electron transition between the valence and conducting bands of inorganic $[Pb_2I_6^{2-}]_\infty$ chain.

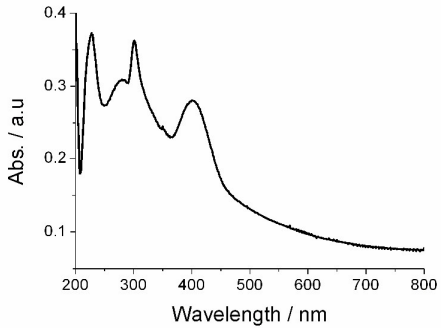

Figure 6 UV-visible absorption spectrum of **1** in solid state at ambient temperature.

It is interesting that the room-temperature photoluminescence (PL) spectra of **1** depend on the excitation wavelengths. As shown in Figure 7, hybrid **1** shows a broad

and weak emission band at room temperature, and this band spans from ca. 400 to 700 nm and is almost across the whole visible spectroscopic region, giving rise to white light emission, when it was excited by the light with λ_{ex}< 370 nm. The photograph of white light emission is shown in the Figure 7c when the powdered sample of **1** was illuminated by a UV lamp (which wavelength ranges from 330 to 380 nm) at ambient temperature. The band center of PL emission red-shift and the emission intensity become stronger as the excitation wavelength increases. The emission band in the long wavelength side extends to 750 nm upon the excitation of λ_{ex}>470 nm, and shows a clear shoulder when λ_{ex}>490 nm. The excitation wavelength dependent emission indicates the existence of several excitation states emitting luminescence in **1**. Theoretically, the pyridyl ring in the cation moiety and the inorganic $[Pb_2I_6^{2-}]_\infty$ chain probably emit luminescence in **1**, on the basis of the absorption spectrum of **1** in solid state, the π* level of pyridyl ring is over the conducting band level of inorganic $[Pb_2I_6^{2-}]_\infty$ chain. Thus, the emission band in the shorter wavelength region with the maximum of λ_{em} = 453 nm (see the sect of the low temperature luminescence at 10 K) is attributed to the π←π* transition within the pyridyl ring and the emission bands in the longer wavelength region with the band maximum of λ_{em}>500 nm contribute from the emission of the intrinsic and trap state of $[Pb_2I_6^{2-}]_\infty$ inorganic twin chain. The trap states are related to the lattice defects. The pyridyl ring emitting weak fluorescence is due to the existence of π…π stacking interaction between them (see the crystal structure section), such π…π stacking interactions lead to the stacked pyridyl rings easily forming the excimers, which quench fluorescence. With respect to the emission using longer wavelength light excitation (λ_{ex}> 470 nm, ref. Figure 7a), the emission arising from the intrinsic and trap state of inorganic $[Pb_2I_6^{2-}]_\infty$ chain of **1** is also weak when it was excited by the light with λ_{ex}< 470 nm, this fact discloses the presence of absent efficient energy transfer process between the higher π* level of pyridyl ring and the lower conducting band level and the trap state level of $[Pb_2I_6^{2-}]_\infty$ inorganic twin chain.

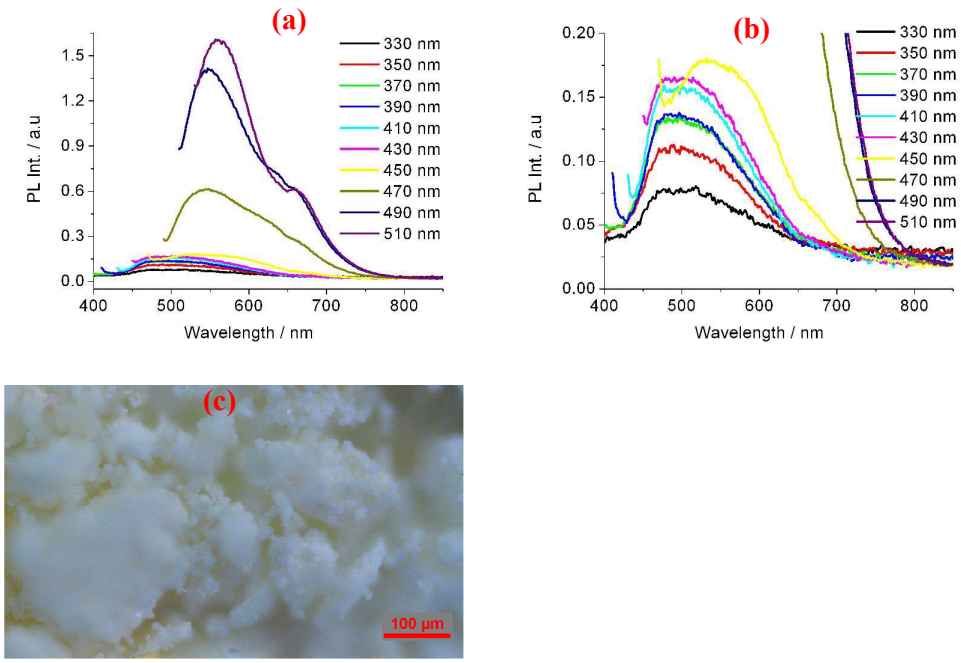

Figure 7 (a) Solid-state PL spectra of **1** at room temperature and under variation of excited light (b) enlarged one showing the emission upon shorter wavelength excitation (λ_{ex}≤450 nm) and (c) photographs of powered sample of **1** showing white-light emission at 296 K under UV lamp with wavelength of 330-380 nm.

Hybrid **1** shows not only the excitation light wavelength-dependent but also the temperature-dependent emission spectra. Figure 8a shows temperature-dependent PL spectra of **1** at selected temperatures, the intensities of emission bands centered at 453 nm and 547 nm increases as temperature lowered. Moreover, the relative intensity between two emission bands changes with temperature variation. It is noted that, for example, the emission bands at 453 nm and 547 nm are comparable in intensity when λ_{ex} = 330 nm at 223 K, this gives rise to nearly white light with CIE coordinates of (0.33, 0.36) and CCT of 5611 K (the CIE coordinates are (0.33, 0.33) for pure white light). Under the same excitation wavelength, when T = 173 K, the band with maximum at 547 nm is more intense than the band centered at 453 nm, besides this difference, even if the emission is located in the white-light region, the CIE coordinates moves to (0.35, 0.41).

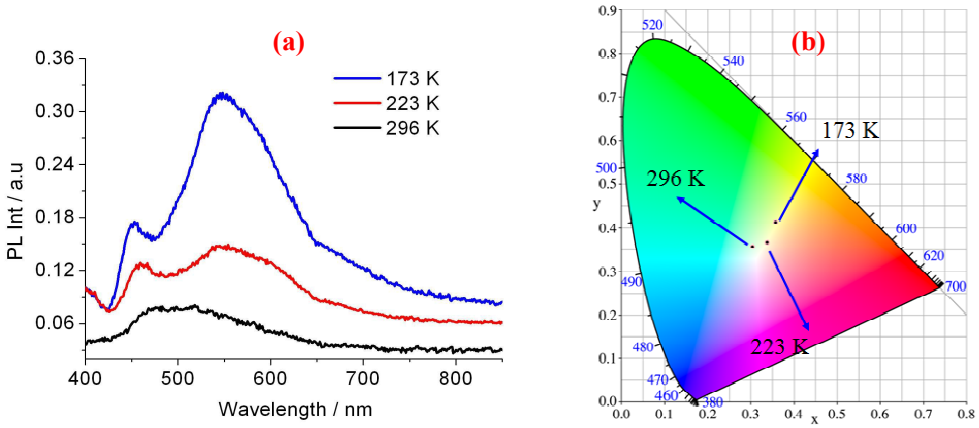

Figure 8 (a) Solid state emission spectra at selected temperatures (b) CIE 1931 chromaticity diagram at 296, 223 and173 K.

Discussion

In the ion-type hybrid **1**, the whole conductivity obtained from the impedance measurement contributes from both electron transport and ion conduction. It was demonstrated experimentally that the dark conductivity of PbI_2 crystals with layered structure was distinction along different crystallographic axes. Dark conductivities of the PbI_2 crystal were $5.9\times10^{-10}$and 7.1×10^{-12} $S\cdot cm^{-1}$ at room temperature, when the electrical field was applied perpendicular (within intra-layer of PbI_2) and parallel (between inter-layer of PbI_2) to the *c*-axes of crystal,[31] respectively. The main pathway of electron transport in **1** is through the inorganic $\{Pb_2I_6\}_\infty$ twin chain. With respect to the 2-D PbI_2 crystal, the conductivity contributed from electron transport should be much lower in **1** owing to the only existence of discrete $\{Pb_2I_6\}_\infty$ twin chains. On the other hand, the conductivity contributing from electron transport can be gotten from DC electrical measurement, and theoretically, the conductivity obtained from AC measurement should be close to that gained from DC measurement when the applied AC frequency is close to zero. The conductivity of **1** is 3.55×10^{-12} $S\cdot cm^{-1}$ at 293 K when f = 1 Hz, which is still comparable to the electrical conductivity of PbI_2 crystal at room temperature. The results disclose that the ion conduction plays an important role in the electrical conducting mechanism of **1**.

On the basis of the structural analysis, it is found that the significant lattice expansion occurs across the structural phase transition and the cations show heavily

dynamic disorder from LT to HT phase, these observations confirm the orientation and displacement motions being more favor under an applied electrical field in HT phase regarding LT phase. The cation mobility enhancing in HT phase responds to the conductivity jump from LT to HT phase.

Up to date, the compounds with switchable magnetic or optical nature through thermally induced structure change have been widely studied,[21,32,33] on the other hand, although the switchable conductivity materials were discovered most in inorganic semiconductors[34-37] and a few of polymers or organic supramolecular compounds, and in later case, the switchable conductance is related to the conformational changes or elcetroreduction,[38-40] to the best of our knowledge, hybrid **1** is the first example showing switchable ion conductance in hybrid materials.

In the context of white-light emission material, white light semiconductor nanocrystals have being widely studied and became a class of promisingly useful white-light emission material. However, most of them require the specialized processing techniques for preparation. Regarding the complicated process of preparation for semiconductor nanocrystals, this hybrid is formed in solution using a simple self-assembly approach. In addition, most of white lighting emission materials are generally produced by combination of different emitters (red/blue/green or blue/orange) to cover the visible range from 400 to 700 nm, obviously, the drawback of such a multi-phase strategy is fabricating complication and high-cost problems of device.[41-44] Thus, it is desirable to develop the single-phase white light emitter which is enable easy fabrication with perfect color reproducibility and stability. Single-phase emitters have been discovered in organic compound[45-48] and metal complexes,[49-54] however, scarce in the organic-inorganic hybrid semiconductor.[55-58]

Conclusion

In summary, we have successfully achieved an iodoplumbate-based hybrid using a simple self-assembly approach in solution. This hybrid shows switchable ion conductance, resulting from the structural phase transition, as well as both excitation light wavelength- and temperature-dependent photoluminescence behaviors. The

excitation light wavelength-dependent photoluminescence arises from the multiple band emission, which originate from the π←π* transition within the pyridyl ring of cation and the electron transition between the valence and conducting bands of inorganic $[Pb_2I_6^{2-}]_\infty$ chain. The white-light emission was achieved via illuminated by a UV lamp with light wavelength of 330-380 nm at room temperature and excited by λ_{ex} = 330 nm at 223 K. To the best of our knowledge, this is the first example that a crystalline hybrid semiconductor displays the features of both white-light emission and switchable ion conductance. Our result offers promising prospects for creating molecular crystal potentially applied in switchable ion conductor device and high-efficiency lighting-emitting diodes.

Experimental section

Chemicals and materials

All chemicals and solvents were reagent grade, and used without further purification. [C_7-Apy]Br was prepared using a similar method reported in our previous studies.[37]

Preparation of 1

A mixture of PbI_2 (0.926 g, 2 mmol) and KI (3.320 g, 20 mmol) with molar ratio of 1:10 in DMF (50 mL) was heated under reflux with stirring for 25 min. After the clear yellow solution was formed and a DMF solution [C_7-Apy]Br (0.546 g, 2 mmol) was slowly added to the mixture, which was stirred for 4 h and filtered to remove insoluble compounds. The filtrate was evaporated at ambient temperature to produce light yellowish needle-shaped crystals in ca. 70% yield. Anal. Calcd for $C_{24}H_{41}I_6N_4Pb_2$: C, 18.46; H, 2.64; N, 3.58. Found: C, 18.20; H, 2.43; N, 3.73.

Physical measurements

Elemental analyses for C, H and N were performed with an Elementar Vario EL III analytic instrument. Power X-ray diffraction (PXRD) data were collected on a Riga-Ku/max-2550 diffractometer with Cu Kα radiation (λ = 1.5418 Å).

Thermogravimetric (TG) experiments were performed with a TA2000/2960 thermogravimetric analyzer from 283 K to 873 K at a warming rate of 10 K/min under a nitrogen atmosphere, and the polycrystalline samples were placed in an aluminum crucible. Differential scanning calorimetry (DSC) was carried out on Pyris 1 power-compensation differential scanning calorimeter for **1** and the warming rate is 10 $K \cdot min^{-1}$ during the heating process. The solid-state fluorescence measurements were performed at 298, 223, 173 and 10 K on Fluorolog-3-tau spectrofluorimeter. Temperature and frequency dependent dielectric permittivity and AC impedance measurements were carried out employing Concept 80system (Novocontrol, Germany) in the ranges of 173-413 K; the powdered pellet, with a thickness of ca. 0.66 mm and 132.6 mm2inthe area, was coated by gold films on the opposite surfaces and sandwiched by the copper electrodes and the ac frequencies span from 1 Hz to 10^7 Hz.

X-ray single crystallography

The diffraction data were collected for the same crystal with graphite monochromated Mo Kα (λ = 0.71073 Å) on a CCD area detector (Bruker-SMART) for **1** at 296, 393and 421 K (heating mode). Data reductions and absorption corrections were performed with the SAINT and SADABS software packages,[59] respectively. Structures were solved by the direct method and refined by the full-matrix least-squares procedure on F^2 using SHELXL-97 program.[60] The non-Hydrogen atoms were anisotropically refined, and the hydrogen atoms were introduced at calculated positions for crystals **1** at 296 and 393 K. It is mentioned that it is really difficult to obtain good data of single crystal X-ray diffraction in HT phase since the structure is heavily disorder upon heating. Disordered models for carbon atom of alkyl chain were used in the structure refinements of **1** at 421 K; the occupied factors of the C atoms were refined, while they were not refined anisotropically and the H atoms were not attached. In addition, the pyridyl rings were fixed using the model of six atoms being co-plane in the refinement. The crystallographic details about data collection and structural refinement are summarized in Table S1. Selected bond lengths and angles for 1at 296, 393 and 421 K together with their estimated

standard deviations are listed in Table S2.

Acknowledgements

The authors thank the Priority Academic Program Development of Jiangsu Higher Education Institutions and National Nature Science Foundation of China for financial support (grant no. 91122011 and 21201103).

Supplementary Information

Crystallographic data in CIF format and the profiles of PXRD, TG, emission spectra in solids at 10, 173, 223 and 296 K and dielectric permittivity for **1** in PDF format are available free of charge via the Internet at

References

1. S. P. Zhao, X. M. Ren, *Dalton Trans*. **2011**, *40*, 8261-8272.
2. H. Krautscheid, F. Vielsack, *Angew. Chem. Int. Ed*. **1995**, *34*, 2035-2037.
3. H. Krautscheid, C. Lode, F. Vielsack, H. Vollmer, *J. Chem. Soc. Dalton Trans.* **2001**, 1099-1104.
4. Z. Tang, A. M. Guloy, *J. Am. Chem. Soc*. **1999**, *121*, 452-453.
5. J. J. Liu, Y. F. Guan, C. Jiao, M. J. Lin, C. C. Huang, W. X. Dai, *Dalton Trans.* **2015,** 44, 5957-5960.
6. Z. J. Zhang, S. C. Xiang, Y. F. Zhang, A. Q. Wu, L. Z. Cai, G. C. Guo, J. S. Huang, *Inorg. Chem*. **2006**, *45*, 1972-1977.
7. A. Lemmerer, D. G. Billing, *CrystEngComm*. **2012**, *14*, 1954-1966.
8. R. D. Willett, K. R. Maxcy, B. Twamley, *Inorg. Chem.* **2002**, *41*, 7024-7030.
9. E. R. Dohner, E. T. Hoke, H. I. Karuadasa, *J. Am. Chem. Soc.* **2014**, *136*, 1718-1721.
10. C. Wehrenfenging, M. Liu, H. J. Snaith, M. B. Johnston, L. M. Herz, *J. Phys. Chem. Lett.* **2014**, *5*, 1300-1306.
11. A. M. Guloy, Z. J. Tang, P. B. Miranda, V. I. Srdanov, *Adv. Mat.* **2001**, *13*, 833-837.
12. J. I. Fujisawa, T. Ishihara, *Phys. Rev. B*, **2004**, *70*, 113203-113024.
13. G. N. Liu, J. R. Shi, X. J. Han, X. Zhang, K. Li, J. Li, T. Zhang, Q. S. Liu, Z. W. Zhang, C. C. Li, *Dalton Trans.* **2015,** 44, 12561-12575.
14. W. S. Yang, J. H. Noh, N. J. Jeon, Y. C. Kim, S. Ryu, J. Seo, S. I. Seok, *Science* **2015**, *348*,1234.
15. M. Liu, M. B. Johnston, H. J. Snaith, *Nature* **2013**, *501*, 395-398.
16. G. Xing, N. Mathews, S. Sun, S. S. Lim, Y. M. Lam, M. Grätzel, S. Mhaisalkar, T. C. Sum, *Science* **2013**, *18*, 344-347.
17. E. J. Yoo, M. Lyu, J.-H. Yun, C. J. Kang, Y. J. Choi, L. Wang, *Adv. Mater.* **2015**, *27*, 6170–6175.
18. H. R. Zhao, D. P. Li, X. M. Ren, Y. Song, W. Q. Jin, *J. Am. Chem. Soc*. **2010**, *132*,

18-19.

19. Z. J. Zhang, S. C. Xiang, G. C. Guo, G. Xu, M. S. Wang, J. P. Zou, S. P. Guo, J. S. Huang, *Angew. Chem. Int. Ed.***2008**, *47*, 4149-4152.
20. P. Maldonado, S. Kanungo, T. Saha-Dasgupta, P. M. Oppeneer, *Phys. Rev. B,* **2013**, *88*, 020408.
21. O. Kahn, C. J. Martinez, *Science* **1999**, *279*, 44-48.
22. J. Liang, Z. Chen, L. Xu, J. Wang, J. Yin, G. A. Yu, Z. N. Chen, S. H. Liu, *J. Mater. Chem. C***2014**, *2*, 2243-2250.
23. X. Y. Dong, B. Li, B. B. Ma, S. J. Li, M. M. Dong, Y. Y. Zhu, S. Q. Zang, Y. Song, H. W. Hou, T. C. W. Mak, *J. Am. Chem. Soc.***2013**, *135*, 10214-10217.
24. J. E. Bauerle, *J. Phys. Chem. Solids* **1969**, *30*, 2657-2670.
25. A. Hooper, *J. Phys. D: Appl. Phys.***1977**, *10*, 1487-1496.
26. D. Umeyama, S. Horike, M. Inukai, T. Itakura, S. Kitagawa, *J. Am. Chem. Soc.* **2012**, *134*, 12780-12785.
27. I. M. Hodge, M. D. Ingram, A. R. West, *J. Electroanal. Chem. Interfacial Electrochem.* **1976**, *74*, 125-143.
28. I. M. Hodge, M. D. Ingram, A. R. West, *J. Electroanal. Chem. Interfacial Electrochem.* **1975**, *58*, 429-432.
29. H. B. Duan, X. M. Ren, J. L. Liu, *Soft Mater*. **2014**, *12*, 166-178.
30. A. Lemmerer, D. G. Billing, *CrystEngComm*. **2012**, *14*, 1954-1966.
31. Y. Dmitriev, P. R. Bennett, L. J. Cirignano, M. Klugerman, K. S. Shah, *Nucl. Instr. and Meth. Phys. A***2008**, *592*, 334-345.
32. M. C. Muñoz, J. A. Real, *Coord. Chem. Rev*. **2011**, *255*, 2068-2093.
33. R. Ohtani, K.Yoneda, S. Furukawa, N. Horike, S. Kitagawa, A. B. Gaspar, M. C. Muñoz, J. A. Real, M. Ohba, *J. Am. Chem. Soc*. **2012**, *133*, 8600-8605.
34. S. R. Ovshinsky, *Phys. Rev. Lett*. **1968**, *21*, 1450-1452.
35. S. Lang, T. Nilges, *Chem. Mater*. **2006**, *18*, 2538-2544.
36. W. R. Hiatt, T. W. Hickmott, *Appl. Phys. Lett*. **1965**, *6*, 106-107.
37. F. Argall, *Solid-State Electron* **1968**, *11*, 535-541.
38. D. Ma, M. A. Aguiar, J. A. Freire, I. A. Hümmelgen, *Adv. Mater*. **2000**, *12*,

1063-1066.

39. T. Ha, J. Glass, T. Enderle, D. S. Chemla, S. Weiss, *Phys. Rev. Lett*. **1998**, *80*, 2093-2096.
40. A. Bandyopadhyay, A. J. Pal, *Appl. Phys. Lett*. **2004**, *84*, 999-1001.
41. P. Bairi, B. Roy, P. Chakraborty, A. K. Nandi, *ACS Apply. Mater. Interface* **2013**, *5*, 5478-5485.
42. G. Tu, C. Mei, Q. Zhou, Y. Cheng, Y. Geng, L. Wang, S. Ma, X. Jing, F. Wang, *Adv. Funct. Mater*. **2006**, *16*, 101-106.
43. B. P. Yan, C. C. C. Cheung, S. C. F. Kui, H. F. Xiang, V. A. L. Roy, S. J. Xu, C. M. Che, *Adv. Mater*. **2007**, *19*, 3599-3603.
44. J. L. Wu, G. Gundiah, A. K. Cheetham, *Chem. Phys. Lett*. **2007**, *441*, 250-254.
45. Q. Y. Yang, J. M. Lehn, *Angew. Chem. Int. Ed*. **2014**, *53*, 1-7.
46. Y. S. Zhao, H. Fu, F. Hu, A. Peng, W. Yang, J. Yao, *Adv. Mater*. **2008**, *20*, 79-83.
47. P. Nanhikonda, M. D. Heagy, *Chem. Comm*. **2010**, *46*, 8002-8004.
48. Y. Yang, M. Lowry, C. M. Schowalter, S. O. Fakayode, J. O. Escobedo, X. Xu, H. Zhang, T. J. Jensen, F. R. Fronczek, I. M. Warner, R. M. Strongin, *J. Am. Chem. Soc*. **2006**, *128*, 14081-14092.
49. C. Y. Sun, X. L. Wang, X. Zhang, C. Qin, P. Li, Z. M. Su, D. X. Zhu, G. G. Shan, K. Z. Shao, H. Wu, J. Li, *Nat. Comm*. **2013**, *4*, 317-324.
50. Y. Zhou, B. Yan, *Inorg. Chem*. **2014**, *53*, 3456-3463.
51. Y. Wada, M. Sato, Y. Tsukahara, *Angew. Chem. Int. Ed.***2006**, *45*, 1925-1928.
52. P. Coppo, M. Duati, V. N. Kozhevnikov, J. W. Hofstraat, L. D. Cola, *Angew. Chem. Int. Ed.* **2005**, *117*, 1840-1844.
53. H. J. Bolink, F. D. Angelis, E. Baranoff, C. Klein, S. Fantacci, E. Coronado, M. Sessolo, K. Kalyanasundaram, M. Grätzel, M. K. Nazeeruddin, *Chem. Commun.* **2009**, *45*, 4672-4674.
54. G. J. He, D. Guo, C. He, X. L. Zhang, X. W. Zhao, C. Y. Duan, *Angew. Chem. Int. Ed.* **2009**, *48*, 6132-6135.
55. E. R. Dohner, E. T. Hoke, H. I. Karuadasa, *J. Am. Chem. Soc.* **2014**, *136*, 1718-1721.

56. X. M. Fang, M. Roushan, R. B. Zhang, J. Peng, H. P. Zeng, J. Li, *Chem. Mater.* **2012**, *24*, 1710-1717.
57. M. Roushan, X. Zhang, J. Li, *Angew. Chem. Int. Ed.* **2012**, *51*, 436-439.
58. G. E. Wang, G. Xu, M. S. Wang, M. S. Wang, L. Z. Cai, W. H. Li, G. C. Guo, *Chem. Sci.* **2015,** 6, 7222-7226.
59. Software packages SMART and SAINT, Siemens Analytical X-ray Instrument Inc., Madison, WI, 1996.
60. G. M. Sheldrick, SHELX-97, Program for the refinement of crystal structure, University of Göttingen, Germany, 1997.

TOC

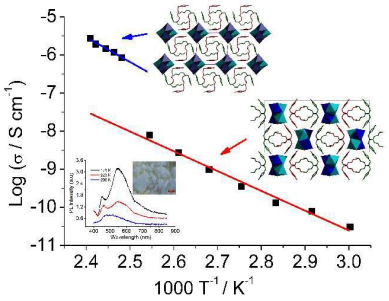

A $[Pb_2I_6]_\infty$ twin chain hybrid crystal shows novel switchable ion conductivity arose from the structural phase transition and color-tunable photoluminescence attributed to the broadband semiconductor emission of twin chain.